ADVANCED FUNCTIONAL MATERIALS
www.afm-journal.de

Discovery of an Intrinsic Antiferromagnetic Semiconductor $EuSc_2Te_4$ With Magnetism-Driven Nonlinear Transport

Seng Huat Lee, Yufei Zhao, Noble Gluscevich, Hemian Yi, Zachary Morgan, Huibo Cao, Jahyun Koo, Yu Wang, Jingyang He, Venkatraman Gopalan, Yuanxi Wang, Weiwei Xie, CuiZu Chang, Qiang Zhang,* Binghai Yan,* and Zhiqiang Mao**

Magnetic topological materials have recently emerged as a promising platform for studying quantum geometry by the nonlinear transport in thin film devices. In this work, an antiferromagnetic (AFM) semiconductor $EuSc_2Te_4$ as the first bulk crystal that exhibits quantum geometry-driven nonlinear transport is reported. This material crystallizes into an orthorhombic lattice with AFM order below 5.2 K and a bandgap of less than 50 meV. The calculated band structure aligns with the angle-resolved photoemission spectroscopy spectrum. The AFM order preserves combined space-time inversion symmetry but breaks both spatial inversion and time-reversal symmetry, leading to the nonlinear Hall effect (NLHE). Nonlinear Hall voltage measured in bulk crystals appears at zero field, peaks near the spin-flop transition as the field increases, and then diminishes as the spin moments align into a ferromagnetic order. This field dependence, along with the scaling analysis of the nonlinear Hall conductivity, suggests that the NLHE of $EuSc_2Te_4$ involves contributions from quantum metric, in addition to extrinsic contributions, such as spin scattering and junction effects. Furthermore, this NLHE is found to have the functionality of broadband frequency mixing, indicating its potential applications in electronics. This work reveals a new avenue for studying magnetism-induced nonlinear transport in magnetic materials.

1. Introduction

The study of the nonlinear Hall effect (NLHE) has garnered significant attention recently[1–10] due to its profound implications for both fundamental physics and technological applications. Materials exhibiting NLHE can convert a longitudinal alternating current (AC) into two Hall voltage components: a rectified direct current (DC) voltage and a second harmonic AC voltage. NLHE can have either intrinsic or extrinsic origins. Intrinsic NLHE is tied to the quantum geometry of electron wave functions,[1,11–15] while extrinsic NLHE stems from disorder scattering.[16–19] Intrinsic NLHE offers a platform to explore novel physics related to quantum geometry, a core feature of topological materials. Due to its quantum mechanical foundation, the rectification process driven by NLHE occurs with an exceptionally fast response time compared to conventional diode-based

S. H. Lee, Y. Wang, Y. Wang[++], Z. Mao
2D Crystal Consortium
Materials Research Institute
The Pennsylvania State University
University Park
PA 16802, USA
E-mail: shl12@psu.edu; zim1@psu.edu

S. H. Lee, N. Gluscevich[+], H. Yi, Y. Wang, Y. Wang[++], C. Chang, Z. Mao
Department of Physics
The Pennsylvania State University
University Park
PA 16802, USA

The ORCID identification number(s) for the author(s) of this article can be found under https://doi.org/10.1002/adfm.202424231

[+]Present address: Department of Physics and Astronomy, Louisiana State University, Baton Rouge, LA 70803, USA

[++]Present address: Department of Physics, University of North Texas, Denton, TX 76201, USA

DOI: 10.1002/adfm.202424231

Y. Zhao, J. Koo, B. Yan
Department of Condensed Matter Physics
Weizmann Institute of Science
Rehovot 7610001, Israel
E-mail: binghai.yan@psu.edu

Z. Morgan, H. Cao, Q. Zhang
Neutron Scattering Division
Oak Ridge National Laboratory
Oak Ridge, TN 37831, USA
E-mail: zhangq6@ornl.gov

J. He, V. Gopalan, Z. Mao
Department of Materials Science and Engineering
The Pennsylvania State University
University Park, PA 16802, USA

W. Xie
Department of Chemistry
Michigan State University
East Lansing, MI 48824, USA

rectification, making it highly promising for high-sensitivity broadband terahertz (THz) detection.[7] This breakthrough could pave the way for THz-band communications, a technology anticipated to play a pivotal role in next-generation (6G) wireless networks.

NLHE has been observed in many 2D materials, including bilayer WTe_2,[3] few-layer WTe_2,[4] corrugated bilayer graphene,[5] graphene moiré superlattices,[20] twisted bilayer WSe_2,[21] and $TaIrTe_4$,[6] as well as in a handful of 3D materials, such as $BaMnSb_2$,[8] $Ce_3Bi_4Pd_3$,[22] $Pb_{1-x}Sn_xTe$,[23] and GeTe.[24] In these materials, NLHE originates from the Berry curvature dipole (BCD), which represents the asymmetric distribution of Berry curvature in momentum space. A recent and exciting breakthrough in this field is the discovery of quantum metric-induced NLHE.[9,10] The quantum metric, corresponding to the real part of the quantum geometry tensor, produces a form of NLHE that is independent of scattering time (τ). This scattering-time independence is particularly advantageous for THz detection, as BCD-induced NLHE, which depends on τ, sets a frequency limit at $1/\tau$. To date, quantum metric-induced NLHE has only been demonstrated in the intrinsic antiferromagnetic (AFM) topological insulator $MnBi_2Te_4$.[9,10] However, this effect has been restricted to even-layer thin films of $MnBi_2Te_4$ and is suppressed in odd-layer or bulk samples due to symmetry constraints. The possibility of realizing quantum metric-induced NLHE in a bulk material remains an open question, though theoretical predictions suggest it may be achievable.

In this work, we report the first example of a bulk antiferromagnetic (AFM) material $EuSc_2Te_4$, that exhibits quantum metric-induced NLHE. $EuSc_2Te_4$ is a newly discovered compound through our research and is isostructural to the existing compound $BaSc_2Te_4$, a small-gap semiconductor ($\Delta \approx 0.2$ eV).[25] Our initial motivation for replacing Ba with Eu stemmed from the hypothesis that if $EuSc_2Te_4$ could be synthesized, it might exhibit properties of a magnetic topological material. This is based on Eu's large magnetic moment, which can potentially induce magnetic ordering, as well as its strong spin–orbit coupling (SOC). Strong SOC could possibly induce band inversion, leading to nontrivial band topology. When combined with magnetism, this could result in an intrinsic magnetic topological insulator, similar to $MnBi_2Te_4$, which has garnered significant attention for enabling access to a variety of topological quantum states, such as the quantum anomalous Hall insulator and axion insulator.[26–33] Our synthesis efforts successfully yielded single crystals of $EuSc_2Te_4$. While we did not find $EuSc_2Te_4$ to exhibit topological properties, its AFM ordering leads to a bulk quantum metric-induced NLHE, which can be used for broadband frequency mixing.

Our $EuSc_2Te_4$ crystals were synthesized using the self-flux method. Through single-crystal X-ray diffraction (XRD), magnetometry, and neutron diffraction, we identified an AFM order below 5.2 K, which breaks both inversion and time-reversal symmetry but preserves combined space-time inversion symmetry. Our experiments also revealed that $EuSc_2Te_4$ is a small-bandgap semiconductor with a gap of less than 50 meV. Density functional theory (DFT) calculations predict an inverted bandgap and unquantized axion field under strain, resembling a dynamical axion insulator.[34,35] Remarkably, our experiments show that $EuSc_2Te_4$ bulk crystals exhibit NLHE. As the magnetic field increases, the nonlinear anomalous Hall voltage peaks near the spin-flop transition, then diminishes as the system polarizes into a ferromagnetic state, restoring space inversion symmetry. The coupling between NLHE and the spin-flop transition, along with a scaling analysis of the nonlinear Hall conductivity, indicates that $EuSc_2Te_4$ features intrinsic contributions from the quantum metric alongside extrinsic contributions from spin scattering and junction effects. These findings provide clues for designing new AFM materials with quantum metric-induced NLHE.

2. Results and Discussion

2.1. Crystal Structure and Magnetism of $EuSc_2Te_4$

Single-crystal X-ray diffraction structure refinement found that $EuSc_2Te_4$ crystallizes in the $CaFe_2O_4$ structure type and adopts an orthorhombic structure with the space group *Pnma* (No. 62) (**Figure 1a**). All the ions are located at $y = 0.25$ and $y = 0.75$ planes and occupy the Wyckoff position 4*c*. Similar to the isostructural compounds $SrSc_2Te_4$ and $BaSc_2Te_4$,[25] the Eu ions are bonded in an eight-coordinate geometry to eight Te ions. As shown in Figure 1a, Sc and the six nearest neighboring Te ions form octahedral coordination $[Sc_2Te_4]^{2-}$, forming a chain-like structure along the *b*-axis via octahedral edge sharing. These quasi-1D chains are connected on the *ac*-planes, resulting in a 3D network. The single-crystal diffraction profile can be refined very well with residual factors of $wR_2 = 0.0394$ (see details in the Supporting Information Section S1 for the crystallographic data). Figure S1 (Supporting Information) shows an XRD pattern measured on the flat surface of a $EuSc_2Te_4$ single crystal. All the peaks in this diffraction pattern can be indexed as the (*h*0*l*) reflections in terms of the *Pnma* orthorhombic structure. The sharpness of the diffraction peaks demonstrates the excellent crystallinity of the $EuSc_2Te_4$ crystal. The energy-dispersive X-ray spectroscopy (EDS) composition analysis shows that the grown crystal has a stoichiometric atomic ratio close to $EuSc_2Te_4$ (see Section S2, Supporting Information).

In addition to the structure study, we have also characterized the magnetic and electronic properties of $EuSc_2Te_4$ and found that it is an AFM semiconductor with a narrow direct bandgap. Its antiferromagnetism was revealed from the magnetization and neutron scattering measurements. Figure 1c presents the magnetic susceptibility χ data measured under field-cooled (FC) and zero-field cooled (ZFC) histories with the magnetic field of 100 Oe applied along the *b*-axis and *ac*-plane, respectively. The $\chi(T)$ data exhibits a sharp λ-like transition at 5.2 K for $H//b$; however, for $H//ac$, $\chi(T)$ displays only a small peak at 5.2 K. Such anisotropic temperature dependences of χ, as well as the absence of irreversible behavior in $\chi(T)$ between ZFC and FC, point to an AFM transition with the Néel temperature of $T_N = 5.2$ K. The AFM nature was further revealed in isothermal magnetization measurements, which revealed a spin-flop transition, a typical signature of an AFM state. Figure 1d,e shows the isothermal magnetization data measured at various temperatures with $H//b$ and $H//ac$, respectively. In the configuration of $H//b$ at 2 K, the system undergoes a transition into a metastable canted AFM (CAFM1) state as the field is increased above 0.75 T (H_{c1}) but below 1.45 T (H_{c2}); above H_{c2}, the magnetization becomes

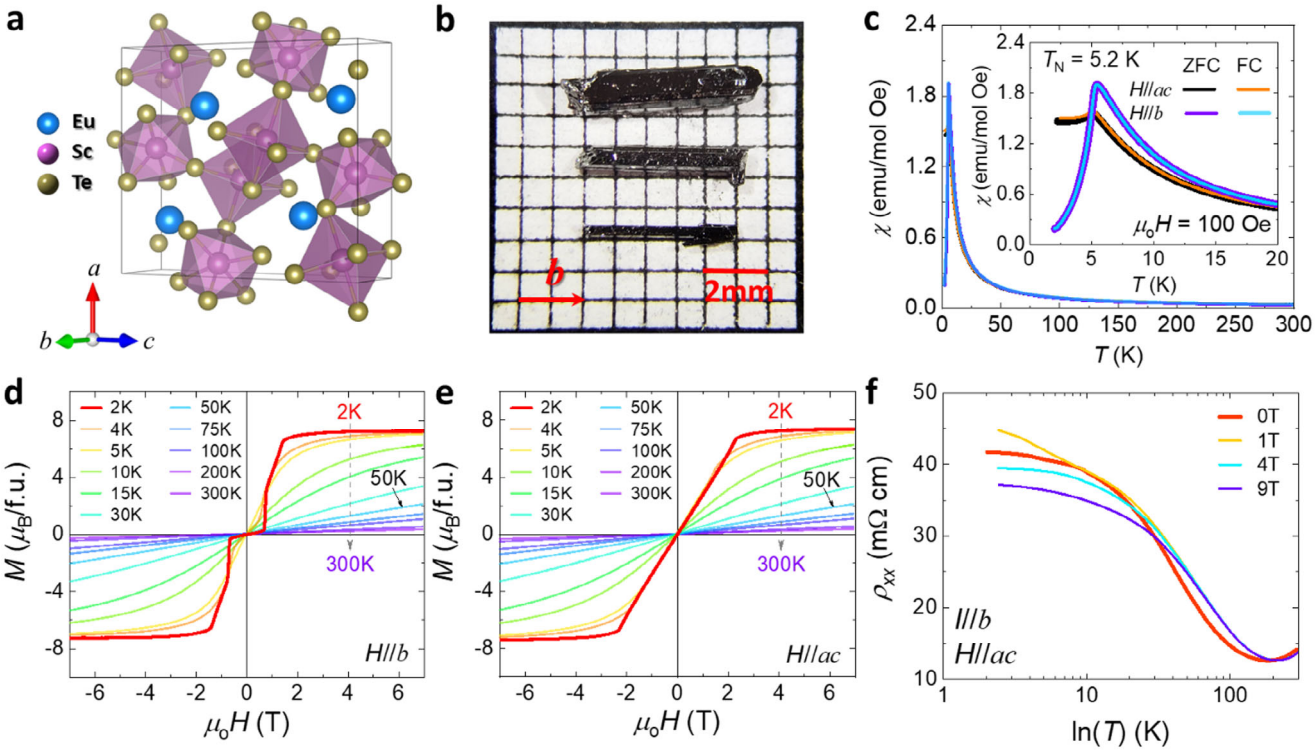

Figure 1. Crystal structure, magnetic, and transport properties of $EuSc_2Te_4$. a) Crystal structure of $EuSc_2Te_4$. b). Optical image of $EuSc_2Te_4$ single crystal. The horizontal arrow indicates the crystallographic *b*-axis. c) Field-cooled (FC) and zero-field cooled (ZFC) temperature dependence of magnetic susceptibility χ measured at 100 Oe for $EuSc_2Te_4$ single crystal aligned with the $H//b$ and $H//ac$ configurations, respectively. Inset: zoomed-in magnetic susceptibility χ in the low-temperature regime. d,e) Isothermal magnetization at various temperatures for the $H//b$ d) and $H//ac$ configurations e). f) Temperature dependences of longitudinal resistivity of $EuSc_2Te_4$ at various magnetic fields.

saturated with the saturation moment of 7.26 μ_B/f.u. These features apparently point to a spin-flop transition. In contrast, for $H//ac$, the measured isothermal magnetization displays an almost linear field dependence, indicating that the AFM state is gradually polarized to a forced ferromagnetic (FM) state above H_c = 2.30 T with the saturated moment of 7.40 μ_B/f.u. These large differences in magnetic polarization between $H//b$ and $H//ac$ imply that the system is magnetically anisotropic with the spin-easy axis along the *b*-axis. Apparently, the AFM order seen in $EuSc_2Te_4$ originates from the magnetic moments of Eu^{2+} ions. The fact that the saturated moment of 7.40 μ_B/Eu probed for $H//ac$ is greater than the free Eu^{2+} moment of 7.0 μ_B indicates the contribution of SOC to the magnetism in $EuSc_2Te_4$. Note that the saturation moment of 7.26 μ_B/Eu probed for $H//b$ indicates that the system is not fully polarized to an FM state even above H_{c2} under the field orientation of $H//b$ but still has a small AFM component up to 7 T (the maximum field in our current measurements). In this case, a secondary metamagnetic transition would be expected at a higher field.

2.2. Magnetic Structural Determination

To further understand the magnetic property, we first calculate the total energies for different spin configurations in **Figure 2a**. The magnetic Eu^{2+} sites are labeled as 14, where ↑/↓ represents the spin orientation. Three collinear AFM and FM orders with the moments parallel to the *a*-, *b*-, and *c*-axis are considered, and corresponding energies are summarized in Table S3 (Supporting Information). Each Eu^{2+} ion tends to have half-filled *f* orbitals with a local moment $|S| = 7\ \mu_B$. Since lattice parameter *b* is shorter than *a* and *c*, the structural anisotropy leads to the magnetic anisotropy. DFT results suggest that an AFM order (↑↑↓↓, the most left panel in Figure 2a) with the easy axis along the *b*-axis is the magnetic ground state of $EuSc_2Te_4$, which is confirmed by our neutron scattering experiment (see below). A small external magnetic field is expected to tune AFM into the FM phase, which is consistent with our experimental observations shown in Figure 1d,e.

Our symmetry analysis based on the refined crystal structure and magnetic structure from neutron diffraction confirms the AFM order with the magnetic space group *Pn'ma* (No. 62.443) in $EuSc_2Te_4$. A representative illustration of the neutron scattering results probed on the (*h*1*l*) plane at 10 and 1.4 K is presented in Figure 2c,d. By comparing the low-*Q* peaks at 10 and 1.4 K, we can identify several magnetic peaks, such as (111), (−111), (202), (−211), (213), (−511), etc. As shown in Figure 2b, the temperature dependence of the nuclear and magnetic peak (202) reveals a magnetic transition at ≈5.2 K, which is in good agreement with the susceptibility measurement result (Figure 1c). The temperature dependence of the (202) peak is fitted using a power law $I(T) \propto (1\text{-}T/T_N)^{2\beta}$, yielding a critical exponent of 0.28. This value is close to those observed in the 3D Ising ($\beta \approx 0.33$) or 3D Heisenberg ($\beta \approx 0.36$) model.[36] At 1.4 K, all the magnetic

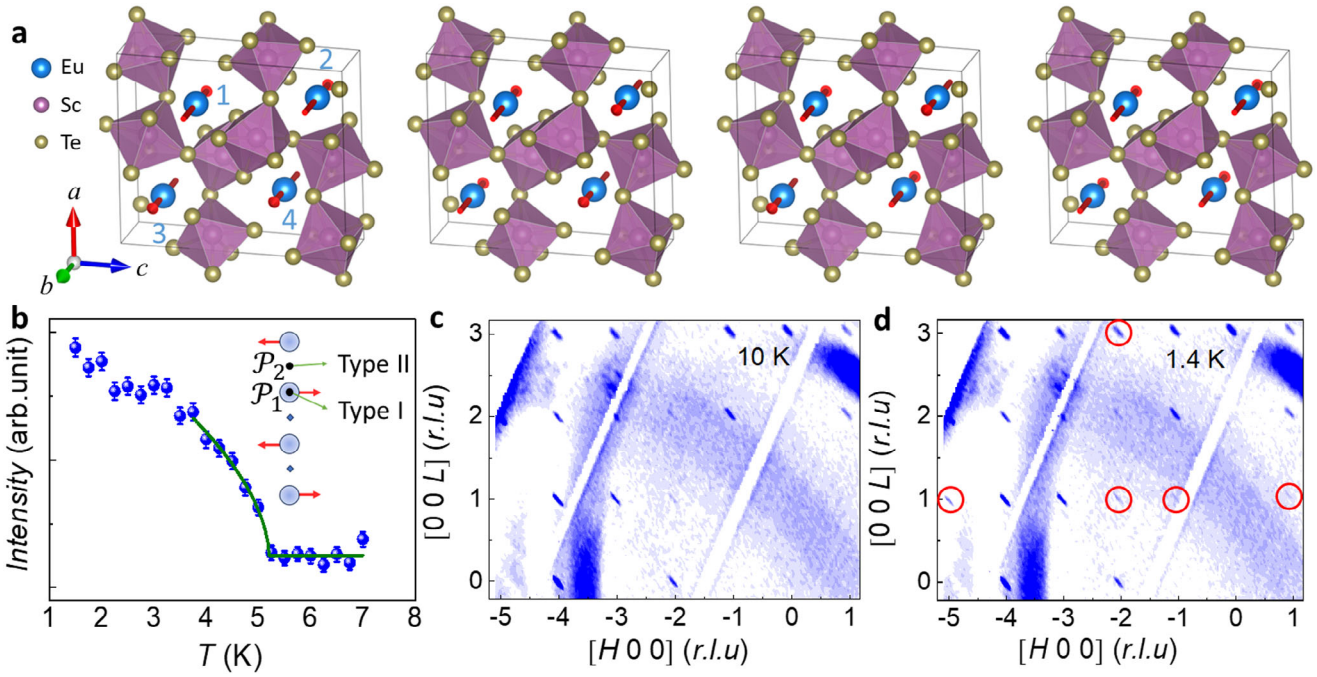

Figure 2. AFM magnetic structure. a) Four possible magnetic structures (see Table S3 (Supporting Information) for details). b) Temperature dependence of the nuclear and magnetic peak (202). The solid line is the fits using the power law (see text). Inset: A carton to illustrate two types of inversion symmetry ($\mathcal{P}$) center. $\mathcal{P}_1$ and $\mathcal{P}_2$ represent inversion centers. c,d) Representative neutron diffraction patterns of the (h1l) plane measured at 10 K c) and 1.4 K d). The red circles in (d) denote antiferromagnetic reflections associated with the ***k***-vector (0, 0, 0).

reflections observed in $EuSc_2Te_4$ can be indexed with the *Pnma* unit cell, indicating a commensurate magnetic propagation vector ($\boldsymbol{k} = 0$). Interestingly, the fits to the squared structure factors of the nuclear and magnetic reflections at 1.4 K, after the neutron absorption corrections (see Figure S3b in the Supporting Information Section S3), reveal an AFM order with the magnetic moments aligned along the *b*-axis. The Eu spins exhibit FM arrangements in the *bc* plane and stacks antiferromagnetically along the *a*-axis, as shown in the most left panel of Figure 2a. The refined value of the ordered moment is ≈6.2(3) μ_B, indicative of Eu^{2+} ions with a spin quantum number of $\boldsymbol{S} = 7/2$ in $EuSc_2Te_4$. The refined value falls below the saturated moment observed in the isothermal magnetization measurements (Figure 1d,e). The discrepancy can be attributed to nonfully accounting for the ordered moment besides spin moments in the neutron measurements. Additionally, the significant neutron absorption by Eu ions poses challenges in adequately compensating for the reduced neutron signal despite diligent efforts in neutron absorption corrections.

A key feature of the AFM state in $EuSc_2Te_4$ is that it breaks both inversion symmetry ($\mathcal{P}$) and time-reversal symmetry ($\mathcal{T}$), while preserving the combined space-time reversal symmetry ($\mathcal{PT}$). This contrasts with the AFM state in bulk $MnBi_2Te_4$, which lacks $\mathcal{PT}$ symmetry. The distinction stems from the different locations of the inversion symmetry centers in these materials. In $MnBi_2Te_4$, the inversion symmetry center (denoted as $\mathcal{P}_1$) is located at the magnetic cation site (Mn^{2+}), whereas in $EuSc_2Te_4$, the inversion center ($\mathcal{P}_2$) lies between the magnetic cations (Eu^{2+}), as illustrated in the inset of Figure 2b. It is the $\mathcal{P}_2$ inversion center that leads to the breaking of $\mathcal{P}$ symmetry as the AFM order develops. As we will demonstrate below, this distinctive AFM state in $EuSc_2Te_4$ is responsible for the observed NLHE.

2.3. Electronic Band Structure Determination

Next, we demonstrate that $EuSc_2Te_4$ is a small bandgap semiconductor. Figure 1f illustrates the temperature-dependent resistivity ρ_{xx} with the current applied along the *b*-axis and the magnetic fields applied parallel to the *ac*-plane. In the temperature range of 300–175 K, $EuSc_2Te_4$ exhibits metallic behavior, evolving to semiconducting behavior below 175 K, with its resistivity being in the range of tens of mΩ cm at low temperatures. In room-temperature Fourier-transform infrared (FTIR) spectroscopy measurements on the *ac*-plane (see Figure S6, Supporting Information), we observed an absence of resonance peak in the transmittance spectrum down to 50 meV, implying the bandgap of $EuSc_2Te_4$ is smaller than 50 meV. These findings indicate that $EuSc_2Te_4$ is a small bandgap semiconductor, consistent with the calculated band structure presented below. Moreover, we also find that its electronic properties are strongly coupled with its magnetism, as manifested in the inverse spin-valve effect induced by the spin-flop transition (see details in Section S4, Supporting Information).

We also conducted angle-resolved photoemission spectroscopy (ARPES) measurements and the DFT calculations on $EuSc_2Te_4$ to determine, if it is an intrinsic magnetic topological candidate. Our ARPES band mapping of $EuSc_2Te_4$ in **Figure 3a** reveals that the chemical potential resides near the top of the bulk valence

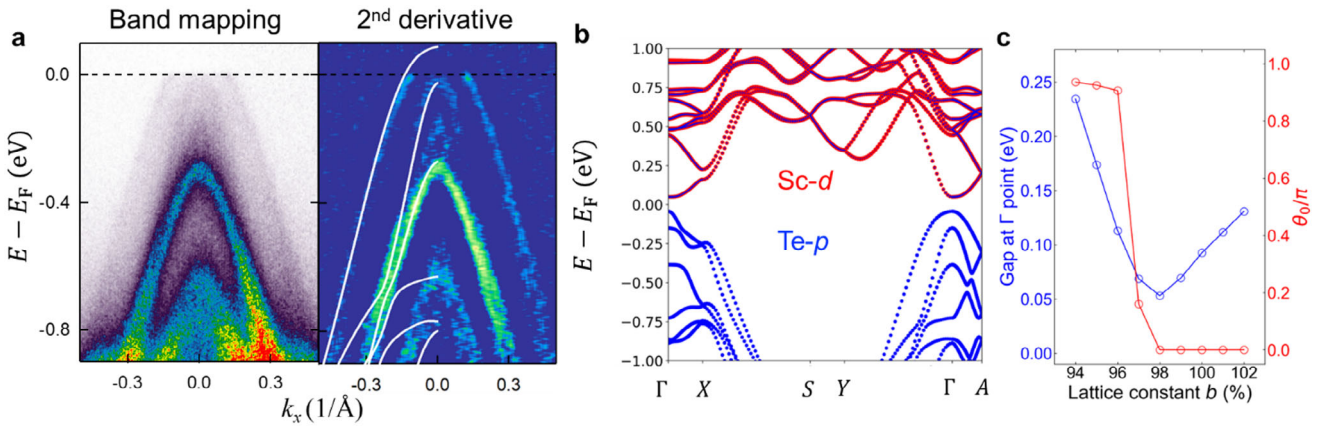

Figure 3. Band structure of $EuSc_2Te_4$. a) Band dispersion along k_x measured by ARPES at 13 K (left) and its second derivative (right). The solid white lines overlaying on the second derivative ARPES spectrum represent the calculated band structure in the AFM state. b) The band structure with the projection of Sc-*d* (red) and Te-*p* (blue) orbitals in the AFM state. c) The evolution of the energy gap at Γ and static axion θ_0 of $EuSc_2Te_4$ with the uniaxial strain along the *b*-axis.

band, consistent with the observed hole doping in the transport measurements (see Figure S4b in the Supporting Information Section S4). Notably, the linear dispersion of the outermost band probed by ARPES is exactly consistent with the DFT calculated electronic structure, as shown in Figure 3a (see the white lines in the right panel). The discrepancy between DFT and ARPES results below 0.6 eV is probably because the ARPES measurements were conducted at 13 K, above T_N (= 5.2 K). The consistency of electronic structure near E_F between the DFT and ARPES results clearly shows that the linearly dispersed bands probed by ARPES is of bulk origin rather than from a topological surface state.

Furthermore, the DFT calculations also suggest that $EuSc_2Te_4$ is in close proximity to a nontrivial topological state. Recall that the magnetic ground state breaks $\mathcal{P}$ and $\mathcal{T}$ but preserves $\mathcal{PT}$, each energy band is doubly degenerate while the nonsymmophic symmetries enforce a fourfold representation along *S*-*Y*. Electronic states near the Fermi level are mainly from Sc-*d* and Te-*p* orbitals, while Eu-*f* electronic states are localized between −3 and −2 eV (see Figure 3b; and Figure S7a, Supporting Information). A trivial bandgap of 93 meV is identified at Γ point, robust against the choice of Hubbard *U*. Interestingly, we found the gap changes significantly when applying a small uniaxial strain along the *a*-, *b*-, and *c*-axis (see Figure S7b, Supporting Information) while the structure remains mechanically stable. In contrast to $\mathcal{T}$-preserved topological insulators, the AFM order introduces an intrinsic mass term, causing the bandgap of $EuSc_2Te_4$ to decrease to a minimum without closing (e.g., $E_g \approx 53.2$ meV when $b' = 0.98*b$), followed by a monotonically increasing trend (Figure 3c; and Figure S7b, Supporting Information). When $b' < 0.98*b$, the band inversion emerges at Γ point but without mirror Chern number changes by tracing the Wilson loop on the $\{M_b|0, \frac{b}{2}, 0\}$ glide plane (see Figure S7c,S7d, Supporting Information). Meanwhile, the axion field θ, derived from the "topological field theory",[34,35,37] exhibits a continuous change from 0 to 0.906π, demonstrating a dynamical axion field driven by the unique interplay of AFM order and topology in $EuSc_2Te_4$ (see Section S5, Supporting Information).

2.4. Magnetism-Induced Nonlinear Transport

Considering the $\mathcal{PT}$ symmetry of the ground state of $EuSc_2Te_4$, its AFM state is expected to generate NLHE. Our symmetry analysis based on the magnetic space group indicates that three independent nonlinear conductivity tensor components $\sigma_{a;aa}$, $\sigma_{a;bb}$ ($-\sigma_{b;ab}$) and $\sigma_{a;cc}$ ($-\sigma_{c;ac}$) are allowed, while all other components vanish. To test this theoretical prediction, we performed nonlinear transport measurements on $EuSc_2Te_4$ by applying an AC current (I^ω) along the *b*-axis ($I^\omega // b$) on the (101) plane of a typical $EuSc_2Te_4$ sample. This sample has a bar shape with a flat, shiny surface corresponding to the (101) crystalline plane, with the longest dimension along the *b*-axis (see the inset to **Figure** 4a). The second harmonic Hall voltage response is observed without an external magnetic field, both in the transverse direction (i.e., the *x-axis*, which is directed at $\theta = 49.4°$ relative to the *a*-axis) and longitudinal direction (i.e., the *y*-axis, which is almost parallel to the *b*-axis), denoted by $V^{2\omega}_{xyy}$ and $V^{2\omega}_{yyy}$, respectively (see the inset to Figure 4a); both $V^{2\omega}_{xyy}$ and $V^{2\omega}_{yyy}$ are quadratically dependent on the applied current I^ω (Figure 4a) and independent of frequency up to 300 Hz (Figure S8, Supporting Information). This nonlinear transport behavior is also reproduced in another device (see Section S6, Supporting Information).

Given that the *a*-axis is not on the (101) plane and the current may not be applied exactly along the *b*-axis due to the 3D nature of the crystal, the probed $V^{2\omega}_{xyy}$ signal is likely from the combined projected components on the *x*-axis of all the allowed nonlinear Hall voltages, with $V^{2\omega}_{abb}$ being the dominant component in light of the symmetry analysis mentioned above. Although $V^{2\omega}_{bbb}$ should be zero according to the symmetry analysis, the probed $V^{2\omega}_{yyy}$ signal can emerge from the combined projected components on the *y*-axis of other allowed nonlinear Hall voltages due to the misalignment, which accounts for the smaller magnitude of the probed $V^{2\omega}_{yyy}$.

Both temperature and magnetic field dependence measurements of $V^{2\omega}_{xyy}$ and $V^{2\omega}_{yyy}$ suggest that the second-order response observed in $EuSc_2Te_4$ is associated with magnetism. $V^{2\omega}_{xyy}$ and $V^{2\omega}_{yyy}$ start to emerge around 100 K in the paramagnetic (PM) state and

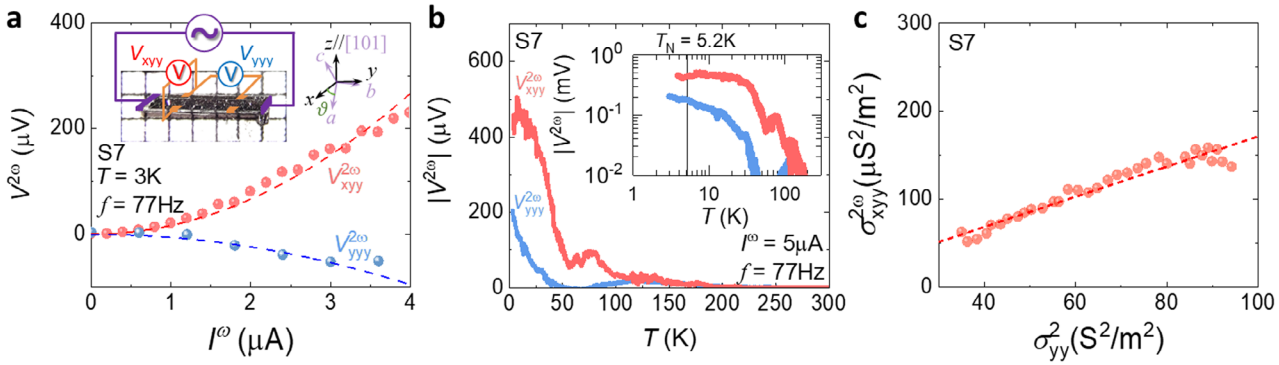

Figure 4. Nonlinear transport of $EuSc_2Te_4$. a) Nonlinear longitudinal $V^{2\omega}_{yyy}$ and transverse $V^{2\omega}_{xyy}$ voltage as a function of input AC current I^{ω} measured at 3 K, 77 Hz in device S7. The red and blue dashed lines are the quadratic fit to $V^{2\omega}_{xyy}$ and $V^{2\omega}_{yyy}$, respectively. The inset shows the experimental setup (left) and the orientation of the crystallographic axes relative to the lab coordinate system. b) Nonlinear longitudinal $V^{2\omega}_{yyy}$ and transverse $V^{2\omega}_{xyy}$ voltage as a function of temperature measured at $I^{\omega} = 5$ μA. Inset: $V^{2\omega}_{yyy}$ and $V^{2\omega}_{xyy}$ data plotted on the logarithmic scale. c) The scaling relationship between the nonlinear Hall conductivity $\sigma^{2\omega}_{xyy}$ and the square of the linear longitudinal conductivity σ_{yy}. The scaling law analysis was carried out within the temperature range of 3–35 K. The dashed line is a fit of the data with the scaling relation $\sigma^{2\omega} = \eta_2 (\sigma^{\omega}_{yy})^2 + \eta_o$.

show a remarkable surge below 50 K due to the presence of short-range magnetic orders as evidenced by isothermal magnetization measurements, and then tends to saturate below T_N, as shown in Figure 4b and its inset. Although the AFM ordering temperature is $T_N = 5.2$ K, the isothermal magnetization data in Figure 1d,e display a sublinear increase with the upward field sweep even for $T_N < T < 50$ K, suggesting that magnetic coupling is present in this temperature range.

Given that the transverse nonlinear Hall conductivity $\sigma^{2\omega}_{xyy}$ can be derived via $\sigma^{2\omega}_{xyy} = J^{2\omega}_{xyy}/(E^{\omega}_{yy})^2 = \frac{V^{2\omega}_{xyy}}{(I^{\omega}_{y})^2 R^3_{yy}} \frac{l^3}{w^2 t}$, where $J^{2\omega}_{xyy}$, E^{ω}_{yy}, R_{yy}, l, w, and t are the second-order current density, longitudinal electric field, linear longitudinal resistance, and the length, width, and thickness of the device, we examined the scaling relationship between $\sigma^{2\omega}_{xyy}$ and the square of the linear longitudinal conductivity σ_{yy} over the temperature range of 3–35 K. In Figure 4c, we find that the $\sigma^{2\omega}_{xyy}$-$(\sigma^{\omega}_{yy})^2$ curve can be well fitted by $\sigma^{2\omega}_{xyy} = \eta_2 (\sigma^{\omega}_{yy})^2 + \eta_o$, where η_o is scattering time τ-independent and $\eta_2(\sigma^{\omega}_{yy})^2$ is the τ^2-dependent term. The τ^2-dependent term is relatively large compared to that in $MnBi_2Te_4$ thin films.[9,10] The nonzero η_o term implies the quantum metric contribution, as discussed below.

Before investigating the possible origins of the nonlinear response, we examine the magnetic field evolution of $V^{2\omega}_{xyy}$ by applying the field parallel and perpendicular to the *b*-axis (see the insets to **Figure 5**b,d), respectively, at 3 K (below T_N). These data clearly demonstrate that the spin-flop and flip transitions significantly influence $V^{2\omega}_{xyy}$. For $H//b$, the system undergoes two spin-flop transitions at H_{c1} and H_{c2}, respectively, as depicted in Figure 5a. $V^{2\omega}_{xyy}$ exhibits a slight increase with the upward field sweep within the AFM phase but shows a striking step-like decrease across the spin-flop transition at H_{c1}, then remains mostly saturated above H_{c2} (Figure 5b). For $H\perp b$, the field-induced gradual spin-flop transition also leads $V^{2\omega}_{xyy}$ to display a maximal value within the canted AFM state and a significant decrease above H_c (Figure 5d).

For both $H//b$ and $H\perp b$, the striking reduction of $V^{2\omega}_{xyy}$ above H_{c2} (H//*b*) or H_c ($H\perp b$) clearly indicates the restoration of $\mathcal{P}$ symmetry when spins are polarized. In the FM or nearly FM state, $V^{2\omega}_{xyy}$ decreases to 41%–51 of its zero field value. The residual nonlinear Hall voltage in the FM phase should be of extrinsic origin, most probably stemming from the junction effect of electric contacts. Our two-probe DC *I*–*V* characteristic measurements provide evidence for the involvement of the junction effect (see Figure S9, Supporting Information).

Compared to the NLHE of the $MnBi_2Te_4$ film,[9,10] $EuSc_2Te_4$ exhibits a distinct feature in the field sweep of $V^{2\omega}_{xyy}$: it does not display a sign reversal upon reversing the direction of the magnetic field. This can be understood in terms of its bulk antiferromagnetism. When a bulk AFM material undergoes a spin-flop transition, its canted AFM state is composed of both AFM and FM components. When the magnetic field is switched from the positive to negative direction, the FM component reverses its direction, as shown in Figure 5a,c, but the wave vector of the AFM component should remain unchanged due to the bulk nature of the antiferromagnetism. In contrast, the AFM wave vector of the even-layer $MnBi_2Te_4$ film can be controlled by the training field, leading to the sign reversal of nonlinear Hall voltage upon switching the magnetic field direction.[9,10] Although the nonlinear Hall voltage output of $EuSc_2Te_4$ (see Figure 4a) appears to be comparable to that of $MnBi_2Te_4$ under the same driving current of 4 μA, $EuSc_2Te_4$'s nonlinear Hall response is much stronger than that of the $MnBi_2Te_4$ flake. This is because the sample used in our measurements is a bulk crystal (≈40 μm thick), much thicker than the $MnBi_2Te_4$ thin flakes (≈2 nm). Given that the nonlinear Hall voltage scales quadratically with the electric field, reducing the thickness of $EuSc_2Te_4$ would lead to a much stronger electric field under the same applied current, resulting in a significantly stronger nonlinear Hall response compared to the $MnBi_2Te_4$ flakes.

After demonstrating the coupling of the second-order response in transport with magnetism in $EuSc_2Te_4$, let's discuss its origin. From the above discussions, it is clear that the second-order response probed in our transport measurements involves not only an extrinsic contribution from junction effects but also a possible intrinsic contribution from band topology.

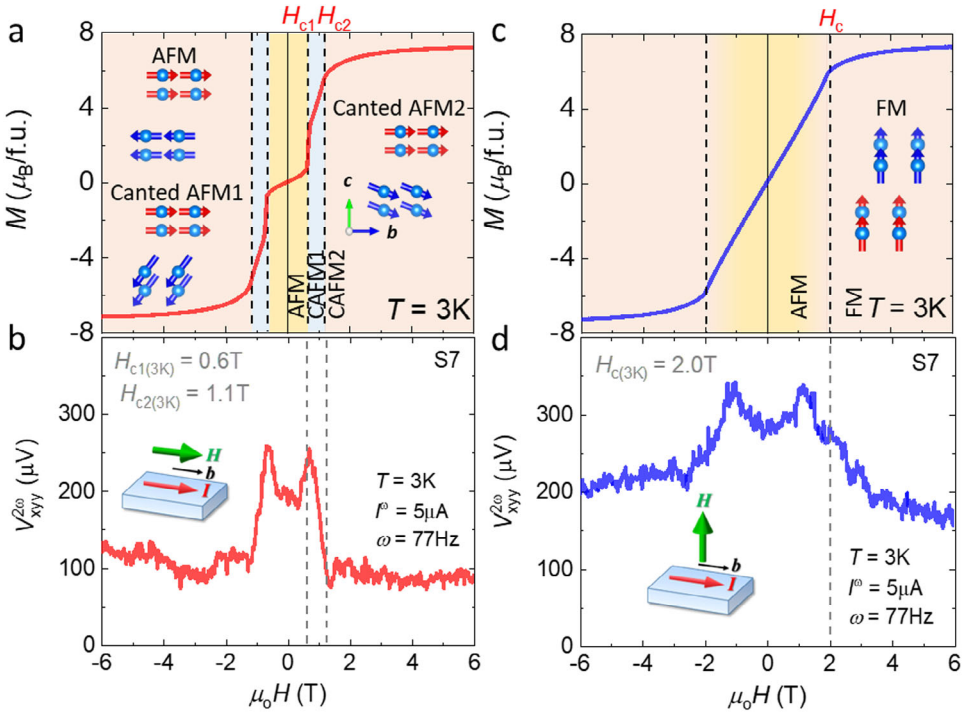

Figure 5. Coupling of nonlinear transport and magnetism in $EuSc_2Te_4$. a,c) Isothermal magnetization at 3 K for the $H//b$ a) and $H//ac$ c) configurations. The insets in (a) and (c) illustrate the antiferromagnetic (AFM), canted antiferromagnetic (CAFM1 and CAFM2), and ferromagnetic (FM) states in the different field ranges. b,d) Nonlinear Hall response $V^{2\omega}_{xyy}$ as a function of field. The insets in (b) and (d) illustrate the experiment setups.

In general, in a uniform, single-domain AFM state with $\mathcal{PT}$ symmetry (e.g., $MnBi_2Te_4$ films[9,10]), the Berry curvature dipole contribution to the second-order response with τ^1-dependence is expected to vanish. Both the scaling analysis of nonlinear Hall conductivity shown in Figure 4c and the calculations of the second-order conductivity shown in Figure S10 (Supporting Information) are consistent with this expectation. Therefore, the intrinsic component of the second-order response probed in $EuSc_2Te_4$, which is coupled with magnetism, should originate from the quantum metric dipole contribution (τ-independent) and Drude contribution ($\propto \tau^2$). This is evidenced by the scaling analysis of the nonlinear Hall conductivity versus the longitudinal conductivity presented in Figure 4c.

Although both the quantum metric and Drude contributions to the Hall conductivity are $\mathcal{T}$-odd and are expected to show sign reversal upon switching the spin moments under magnetic fields, bulk $EuSc_2Te_4$ is not expected to show sign reversal in its intrinsic second-order response as the field is switched from the positive to negative direction. This is because the AFM spin component remains unchanged in its orientations when the field direction is reversed, as discussed above.

Unlike the AFM thin films, which could exhibit a single AFM domain, AFM bulk single crystals like $EuSc_2Te_4$ are usually unavoidable in exhibiting magnetic domains and disorders. Thus, some other extrinsic effects might also be involved in the nonlinear transport. One possible scenario is that the second-order response may also have contributions from spin scattering due to the noncollinear spin canting at domain boundaries. A recently proposed two-spin cluster model[38] suggests $\sigma^{2\omega}$ is proportional to net magnetization and chirality, $\sigma^{2\omega} \propto M\chi$, where $\chi \equiv \langle S_i \times S_j \rangle$ is the vector spin chirality. The reversal of all spin moments will change the sign of both M and χ. This mechanism may account for the peak of $V^{2\omega}_{xyy}$ present at the spin-flop transition for both $H//b$ (Figure 5b) and $H\perp b$ (Figure 5d). Our in-plane magnetoresistivity (MR) measurements (Figure S4a, Supporting Information) clearly show MR peaks at the spin-flop transition, but is strongly suppressed at the fields above the spin-flop transition field, indicating the spin canting significantly increases the scattering rate. Further, the canted AFM state near the spin-flop transition field is most likely characterized by a noncollinear spin structure as seen in the canted AFM state in $MnBi_2Te_4$,[39] which, combined with the increased scattering rate, is expected to enhance the second-order response and result in a peak in $V^{2\omega}_{xyy}$ near the spin-flop transition. Additionally, the side-jump contribution from disorder scattering can also lead to τ^2-dependent second-order response. Given that our nonlinear Hall conductivity scaling analysis presented in Figure 4c has revealed a τ^2-dependent term as shown in Figure 4c, we may need to consider both the side jump contribution due to disorder scattering and the Drude contribution.

Intrinsic NLHE in AFM materials with $\mathcal{PT}$ symmetry holds promising potential, not only for THz detection, as mentioned earlier, but also for applications in AFM spintronics. Prior theoretical studies have suggested that the Néel vector switching, detected by measuring the sign of second-order Hall conductivity in AFM films of CuMnAs,[40,41] is enabled by the quantum metric NLHE. Several other AFM materials, such as CuMnSb, Mn_2Au, $MnPd_2$, PdMnTe,[42,43] have also been predicted to exhibit intrinsic NLHE, although experimental verification is still

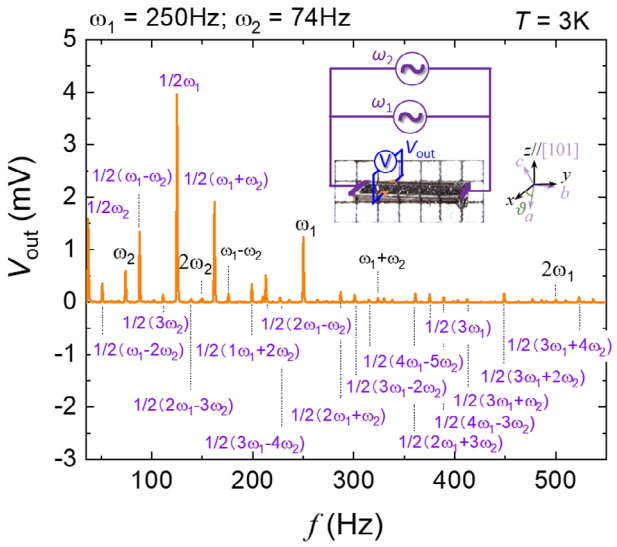

Figure 6. Broadband electronic frequency mixing via NLHE. A mixed frequency spectrum is generated when two AC voltages with nearly identical amplitude but different fundamental frequencies (ω_1 = 250 Hz, ω_2 = 74 Hz) are simultaneously applied to the device. The output voltage exhibits a wide spectrum of mixed frequencies. Black and purple labels indicate the multiple-wave-mixing components and the subharmonic wave-mixing components, respectively. The inset shows a schematic of the experiment setup.

pending. Our findings on intrinsic NLHE in $EuSc_2Te_4$ provide insights for identifying new candidate materials that may display quantum metric-induced NLHE among AFM materials. Specifically, AFM materials where the inversion center is located between magnetic cations break inversion symmetry but preserve $\mathcal{PT}$ symmetry as AFM order develops, which is likely to result in quantum metric-induced NLHE.

2.5. Broadband Electronic Frequency Mixing via NLHE

Recent studies have highlighted the potential of the strong NLHE driven by geometric asymmetric scattering in textured nanoparticles for broadband electronic frequency mixing.[44] In this work, we also demonstrate that the intrinsic NLHE, arising from the quantum metric in $EuSc_2Te_4$, exhibits a similar frequency-mixing capability. To showcase broadband electronic frequency mixing, we connected two voltage sources with nearly identical output amplitudes but different frequencies in parallel to the electrodes along the *y*-axis of the device (see the inset to **Figure 6**). As illustrated in Figure 6, when two alternating voltages of 250 Hz (ω_1) and 74 Hz (ω_2) were applied, we observed 25 distinct frequency peaks in the frequency spectrum of the Hall voltage (*x*-axis), ranging from 35 to 550 Hz. These included sum frequency generation ($\omega_1+\omega_2$), difference frequency generation ($\omega_1-\omega_2$), two second-harmonic frequencies ($2\omega_1$, $2\omega_2$), and 19 subharmonic-wave-mixing components expressed as $(a\omega_1 \pm b\omega_2)/n$, where *a*, *b*, and *n* are positive integers. Notably, the first subharmonic components ($1/2\omega_1$ and $1/2\omega_2$) exhibited the strongest harmonic peaks.

The NLHE origin of the observed frequency mixing was further validated through temperature-dependent measurements. As shown in Figure S11 (Supporting Information), the strong subharmonic wave-mixing components $(a\omega_1 \pm b\omega_2)/n$ persisted up to 150 K, a temperature significantly above the temperature where the short-range magnetic order starts to present (≈50 K). However, the multiple-wave-mixing components $(a\omega_1 \pm b\omega_2)$ were absent at this temperature. This observation suggests that the multiple-wave-mixing components (i.e., $2\omega_1$, $2\omega_2$, $\omega_1+\omega_2$, and $\omega_1-\omega_2$) originate from intrinsic contributions, while the subharmonic wave-mixing components arise from extrinsic effects, such as junction effect. These findings align with our claim of $EuSc_2Te_4$ exhibiting an intrinsic NLHE. While subharmonic wave mixing has previously been proposed and demonstrated in acoustic diodes within nonlinear cavities,[45] our work represents the first demonstration of subharmonic wave mixing in electronic frequency mixing using a single crystal. Although our frequency mixing demonstration is limited to low frequencies, theoretical studies suggest that quantum metric-induced NLHE can persist in the THz regime. A recent study revealed that the NLHE in a type-II Dirac semimetal 1*T*-$CoTe_2$ can occur in a THz regime, though it is caused by an extrinsic mechanism—disorder scattering.[46] Since quantum metric-induced NLHE arises from the quantum geometry of the electron wave function, it is anticipated to be more robust than disorder-driven NLHE and present in the THz regime. However, the demonstration of NLHE in the THz regime for our material would require further systematic investigation, which is beyond the scope of this work.

3. Summary

In summary, we have discovered a novel intrinsic AFM small bandgap semiconducting compound $EuSc_2Te_4$. Through comprehensive studies using X-ray diffraction and neutron scattering, we find this material crystalizes to an orthorhombic structure with the space group *Pnma* (No. 62) and shows an AFM order below 5.2 K. Although this material exhibits a band inversion at Γ point, it does not support a nontrivial topological phase. Nevertheless, its AFM order breaks both $\mathcal{P}$ and $\mathcal{T}$ symmetries but preserves the $\mathcal{PT}$ symmetry. From the nonlinear transport measurements, we found that $EuSc_2Te_4$ exhibits nonlinear Hall responses. Furthermore, the magnetic origin of nonlinear transport is also revealed via the coupling of the nonlinear Hall response to the magnetic field-driven spin-flop transitions. This pronounced nonlinear Hall effect facilitates broadband frequency mixing. In addition, $EuSc_2Te_4$ may also exhibit a large dynamical axion field under pressure. These findings highlight a route to seek nonlinear transport properties and exotic axion physics among bulk AFM materials.

4. Experimental Section

$EuSc_2Te_4$ Single Crystal Growth: Single crystals of $EuSc_2Te_4$ were synthesized using the self-flux method in the Muffle furnaces with instrument DOI:10.60551/yphx-tr33. In an argon atmosphere, the source materials, Eu, Sc, and Te, were mixed in the molar ratio of 1:2:20, with the excessive Te serving as flux. The mixture was placed in an aluminum crucible, evacuated in a sealed quartz tube, heated to 1000 °C for 24 h to promote homogeneous melting, and cooled to 750 °C at 2 °C h^{-1}. Excessive tellurium was removed with centrifugation. Bar-shaped single crystals were obtained with a silver luster using this synthesis procedure. The longest dimension of the crystals is ≈5–6 mm single crystals (see Figure 1b). Growth and

characterization data associated with the samples produced in this study are available via ScholarSphere.[47]

Crystal Structure Study of $EuSc_2Te_4$: The crystal structure of $EuSc_2Te_4$ was determined using a Bruker D8 Quest Eco Single Crystal X-ray Diffractometer equipped with Mo radiation ($\lambda_{K\alpha} = 0.71\,073$ Å) at room temperature. To ensure homogeneity, multiple pieces of crystals (≈20 × 15 × 15 μm^3) from different batches were measured. The crystals were mounted on a Kapton loop and protected by glycerol. Three different crystal and detector orientations were generated to take the measurement with an exposure time of 10 s per frame. The scanning 2θ width was set to 1.7°. Direct methods and full-matrix least squares on F^2 models within the *SHELXTL* package were applied to solve the structure. Data acquisition was obtained via Bruker *SMART* software with the corrections on Lorentz and polarization effect done by *SAINT* program. Numerical absorption corrections were accomplished with *XPREP*. XRD measurements were also performed at room temperature using Malvern Panalytical Empyrean with Cu-K_α radiation to confirm the phase of $EuSc_2Te_4$ crystals for magnetism, electronic transport, and ARPES measurements. The composition of the grown crystals was proven to be $EuSc_2Te_4$ by EDS that covers all the main characteristic peaks of Eu, Sc, and Te at 5.845, 4.088, and 3.769 eV, respectively.

Magnetic Structure and Property Measurements: The magnetic properties of $EuSc_2Te_4$ single crystals were measured using a Quantum Design SQUID magnetometer. Magnetic susceptibility is measured in field-cooled (FC) and zero field-cooled (ZFC) conditions. In the ZFC condition, the measurement was performed in the warming up process at 100 Oe applied magnetic field after the sample was cooled down from 300 K to the desired lowest temperature of 2 K in zero field. The measurements performed in the cooling process under a magnetic field refer to FC measurements.

A single crystal neutron diffraction experiment was carried out at the Dimensional Extreme Magnetic Neutron Diffractometer (DEMAND), located in HFIR, Oak Ridge National Laboratory. A two-axis mode was employed, and the sample was placed in an orange cryostat with a base temperature of 1.4 K. For the measurements, a bar-like piece of crystal with 5 mm length and 0.4 mm lateral size was selected. Neutrons with a wavelength of 1.542 Å using Si-220 monochromator in high-resolution mode (bending 150)[48] were employed for all the measurements. The dataset at 10 K ($>T_N$) and 1.4 K ($<T_N$) were collected. In addition, the temperature dependence of selected nuclear and magnetic peaks was also investigated in the temperature range of 1.4–7 K. Due to the presence of the high neutron absorbing element Eu in the sample, a spherical sample absorption correction was performed on the squared structure factors prior to the data fitting process using the FullProf package.[49] The symmetry-allowed magnetic structures were analyzed via the Bilbao Crystallographic Server.[50]

Electrical Transport Measurements: The transport measurements were performed using a commercial Physical Property Measurement System (PPMS, Quantum Design). The standard four-probe method was used for magnetotransport measurements in which the current is applied along the *b*-axis on the (101) plane. Field sweeps of longitudinal resistivity ρ_{xx} and transverse resistivity ρ_{xy} were conducted for both positive and negative fields. The field dependences of ρ_{xx} and ρ_{xy} are obtained via symmetrizing and antisymmetrizing the data, i.e., $\rho_{xx} = [\rho_{xx}(+\mu_o H) + \rho_{xx}(-\mu_o H)]/2$ and $\rho_{xy} = [\rho_{xy}(+\mu_o H) - \rho_{xy}(-\mu_o H)]/2$, respectively.

Nonlinear Transport Measurements: AC transport measurements are performed by a Keithley 6221 precision AC/DC current source and a Stanford Research SR860 lock-in amplifier. DC measurements were measured by a Keithley 2182A nanovoltmeter. All measurements are carried out with a PPMS to control the temperatures and magnetic fields

ARPES Measurements: ARPES measurements were carried out by cleaving the $EuSc_2Te_4$ single crystals in the ultrahigh-vacuum (UHV) system with a base pressure lower than 5×10^{-11} mbar. The measurements were conducted below 13 K at beamline 5-2 of SSRL, and the hemispherical Omicron-Scienta DA30L analyzer was used. The angular and energy resolution of the DA30L analyzer were set to 0.1° and ≈10 meV, respectively.

Density-Functional Theory and Nonlinear Response Calculations: The first-principles calculations were performed with the Vienna Ab initio Simulation Package (VASP) using the projector-augmented wave method.[51] Given that the crystal and magnetic structures of $EuSc_2Te_4$ are determined, it enables realistic calculations and reveals the main characteristics of its band structure. The exchange-correlation functional based on generalized gradient approximation (GGA) parameterized by Perdew–Burke–Ernzerhof (PBE) was adopted.[52] To treat the correlation effect of localized 4*f* electrons of Eu, the DFT + *U* method by Dudarev et al. was employed.[53] *U* value was tested from 3 to 7 eV. The kinetic energy cutoff of the plane-wave basis was set to 400 eV. Brillouin zone (BZ) integration was performed using a 10×10×10 Γ-centered *k* point mesh to find the magnetic ground state. The maximally localized Wannier functions of Sc-3*d* and Te-5*p* orbitals are built using Wannier90 package.[54] Strain is applied by altering the lattice constant along the loading direction while maintaining the overall symmetry. After modifying the lattice, the atomic positions are relaxed within a tolerance of 10^{-3} eV Å^{-1} to minimize the internal forces and reach an equilibrium ground state.

The second-order conductivity tensor is defined as $j^c = \sigma^{c;ab} E^a E^b$, where *j* is the current response to electric field *E*. *a*, *b*, and *c* is the crystallographic direction. The following formula is next applied to calculate the nonlinear Drude term and the quantum metric term[15]

$$\sigma^{c;ab}(\mu) = -\frac{e^3\tau^2}{\hbar^3}\sum_n \int \frac{d^3k}{(2\pi)^3} f(\varepsilon_n, \mu)\, \partial_{k^a}\partial_{k^b}\partial_{k^c}\epsilon_n - \frac{e^3}{\hbar}\sum_n \int \frac{d^3k}{(2\pi)^3} f(\varepsilon_n, \mu)\left(2\partial_{k^c} G_n^{ab} - \frac{1}{2}\left(\partial_{k^a} G_n^{bc} + \partial_{k^b} G_n^{ac}\right)\right) \quad (1)$$

where $G_n^{ab} = \sum_{m\neq n}\left[\frac{\mathcal{A}_{nm}^a \mathcal{A}_{mn}^b + \mathcal{A}_{nm}^b \mathcal{A}_{mn}^a}{\varepsilon_{nm}}\right]$, $\mathcal{A}_{nm}^i = \langle u_n | \nabla_{k_i} | u_m \rangle$ is the Berry connection, $f(\varepsilon_n,\mu)$ is the Fermi–Dirac distribution, μ is the chemical potential. This integration was performed calculation by applying a 90×300×80 k-mesh.

Dynamical Axion Field: To estimate the axion response in $EuSc_2Te_4$, a low-energy model Hamiltonian based on $|P1_z^+, \uparrow\downarrow\rangle$ and $|P2_{x^2-y^2}^-, \uparrow\downarrow\rangle$ was built. The symmetry operations are given by $\mathcal{PT} = i\sigma_2\tau_3\mathcal{K}$, $C_{2x} = i\sigma_1\tau_0$, $C_{2y} = i\sigma_2\tau_3$. Based on that, Hamiltonian can be written as

$$H(k) = \varepsilon_0(k) + \sum_{a=1}^{5} d_a(k)\,\Gamma_a \quad (2)$$

$$d_{1\sim5}(k) = \left(A_0,\ A_1 k_z, A_2 k_y, M(k), A_3 k_x\right) \quad (3)$$

where $\varepsilon_0(k) = \varepsilon_0 + \varepsilon_1 k_x^2 + M_2 k_y^2 + M_3 k_z^2$, $M(k) = M_0 + M_1 k_x^2 + M_2 k_y^2 + M_3 k_z^2$, and Dirac matrices are $\Gamma_{1\sim5} = (\sigma_1\tau_1, \sigma_2\tau_1, \sigma_3\tau_1, \sigma_0\tau_3, \sigma_0\tau_2)$, which satisfy $\{\Gamma_a, \Gamma_b\} = 2\delta_{ab}$ for $a, b = 1, 2, 3, 4$. A_0 is the mass term to determine the $\mathcal{P}, \mathcal{T}$-symmetry of the system. When $A_0 = 0$ and $M_{1,2,3} > 0$, the system is a topological insulator (or a trivial insulator) if $\frac{M_0}{M_{1,2,3}} < 0$ (or $\frac{M_0}{M_{1,2,3}} > 0$). When $A_0 \neq 0$, $\mathcal{P}, \mathcal{T}$ is breaking but $\mathcal{PT}$ is preserved. The fitting parameters are $\varepsilon_0 = 0.02$ eV, $\varepsilon_1 = -0.005$ eV, $\varepsilon_2 = -0.025$ eV, $\varepsilon_3 = -0.008$ eV, $M_1 = 0.015$ eV, $M_2 = 0.13$ eV, $M_3 = 0.025$ eV, $A_1 = 0.005$ eV Å^{-1}, $A_2 = 0.039$ eV Å^{-1}, $A_3 = 0.01$ eV Å^{-1}. When employing uniaxial strain along b axis (≈94%–102%), M_0 varies in the range [−0.115, 0.061] eV and A_0 varies in [0.001, 0.0266] eV.

For this model, the axion field is given by ref. [35]

$$\theta = \frac{1}{4\pi}\int d^3k \frac{2|d| + d_4}{(|d| + d_4)^2 |d|^3}\epsilon_{ijkl} d_i \partial_x d_j \partial_y d_k \partial_z d_l \quad (4)$$

where *ijkl* takes values from 1, 2, 3, 5.

Supporting Information

Supporting Information is available from the Wiley Online Library or from the author.

Acknowledgements

Y.Z. thanked for the helpful discussion with Zhaochen Liu. The study was based upon research conducted at The Pennsylvania State University Two-Dimensional Crystal Consortium-Materials Innovation Platform (2DCC-MIP), which is supported by NSF Cooperative Agreement No. DMR-2039351. Z.Q.M. also acknowledged the support from NSF under Grant No. DMR 2211327. A portion of this research used resources at the High Flux Isotope Reactor, a DOE Office of Science User Facility operated by the Oak Ridge National Laboratory. The beam time was allocated to DEMAND on Proposal No. IPTS-28766. J.H. and V.G. acknowledged support from the National Science Foundation Grant No. NSF DMR- 2210933. Y.X.W. acknowledged the support from UNT startup funds and DMR-2340733 for providing general research support during the period this work was conducted. The ARPES measurements are partially supported by the Penn State MRSEC for Nanoscale Science (DMR-2011839). C.-Z.C. acknowledged the support from the Gordon and Betty Moore Foundation's EPiQS Initiative (GBMF9063 to C.-Z.C).

Conflict of Interest

The authors declare no conflict of interest.

Author Contributions

S.H.L., B.Y., and Z.Q.M. conceived the project. The crystal growth was carried out by S.H.L., N.G., Y.W., and Z.Q.M. The transport measurements and magnetic measurements were performed by S.H.L. and the analysis was performed by S.H.L. and Z.Q.M. The crystal structure was calculated by Y.X.W. The single crystal XRD study was performed by W.X. The magnetic structure measurements via neutron scattering were carried out by Z.M., H.B., and Q.Z. The FTIR was performed by J.H. and V.G. The electronic structures, magnetic structures, quantum metrics, and dynamical axion field were calculated by Y.Z., J.K., and B.Y. The ARPES study was performed by H.Y. and C.-Z.C. The paper was written by S.H.L. Y.Z., B.Y., and Z.Q.M. with input from all authors.

Data Availability Statement

The data that support the findings of this study are openly available in ScholarSphere at https://data.2dccmip.org/QvPOSeOWU0LG, reference number 47.

Keywords

$EuSc_2Te_4$, intrinsic antiferromagnetic semiconductor, nonlinear Hall effect, quantum metric

Received: January 12, 2025
Revised: February 25, 2025
Published online:

[1] I. Sodemann, L. Fu, *Phys. Rev. Lett.* **2015**, *115*, 216806.
[2] Y. Zhang, Y. Sun, B. Yan, *Phys. Rev. B* **2018**, *97*, 041101.
[3] Q. Ma, S.-Y. Xu, H. Shen, D. MacNeill, V. Fatemi, T.-R. Chang, A. M. Mier Valdivia, S. Wu, Z. Du, C.-H. Hsu, S. Fang, Q. D. Gibson, K. Watanabe, T. Taniguchi, R. J. Cava, E. Kaxiras, H.-Z. Lu, H. Lin, L. Fu, N. Gedik, P. Jarillo-Herrero, *Nature* **2019**, *565*, 337.
[4] K. Kang, T. Li, E. Sohn, J. Shan, K. F. Mak, *Nat. Mater.* **2019**, *18*, 324.
[5] S.-C. Ho, C.-H. Chang, Y.-C. Hsieh, S.-T. Lo, B. Huang, T.-H.-Y. Vu, C. Ortix, T.-M. Chen, *Nat. Electron.* **2021**, *4*, 116.
[6] D. Kumar, C.-H. Hsu, R. Sharma, T.-R. Chang, P. Yu, J. Wang, G. Eda, G. Liang, H. Yang, *Nat. Nanotechnol.* **2021**, *16*, 421.
[7] Y. Zhang, L. Fu, *Proc. Natl. Acad. Sci. USA* **2021**, *118*, 2100736118.
[8] L. Min, H. Tan, Z. Xie, L. Miao, R. Zhang, S. H. Lee, V. Gopalan, C.-X. Liu, N. Alem, B. Yan, Z. Mao, *Nat. Commun.* **2023**, *14*, 364.
[9] N. Wang, D. Kaplan, Z. Zhang, T. Holder, N. Cao, A. Wang, X. Zhou, F. Zhou, Z. Jiang, C. Zhang, S. Ru, H. Cai, K. Watanabe, T. Taniguchi, B. Yan, W. Gao, *Nature* **2023**, *621*, 487.
[10] A. Gao, Y.-F. Liu, J.-X. Qiu, B. Ghosh, T. V. Trevisan, Y. Onishi, C. Hu, T. Qian, H.-J. Tien, S.-W. Chen, M. Huang, D. Bérubé, H. Li, C. Tzschaschel, T. Dinh, Z. Sun, S.-C. Ho, S.-W. Lien, B. Singh, K. Watanabe, T. Taniguchi, D. C. Bell, H. Lin, T.-R. Chang, C. R. Du, A. Bansil, L. Fu, N. Ni, P. P. Orth, Q. Ma, et al., *Science* **2023**, *381*, 181.
[11] Y. Gao, S. A. Yang, Q. Niu, *Phys. Rev. Lett.* **2014**, *112*, 166601.
[12] Y. Tokura, N. Nagaosa, *Nat. Commun.* **2018**, *9*, 3740.
[13] Z. Z. Du, H.-Z. Lu, X. C. Xie, *Nat. Rev. Phys.* **2021**, *3*, 744.
[14] K. Das, S. Lahiri, R. B. Atencia, D. Culcer, A. Agarwal, *Phys. Rev. B* **2023**, *108*, L201405.
[15] D. Kaplan, T. Holder, B. Yan, *Phys. Rev. Lett.* **2024**, *132*, 026301.
[16] S. Nandy, I. Sodemann, *Phys. Rev. B* **2019**, *100*, 195117.
[17] Z. Z. Du, C. M. Wang, S. Li, H.-Z. Lu, X. C. Xie, *Nat. Commun.* **2019**, *10*, 3047.
[18] Z. Z. Du, C. M. Wang, H.-P. Sun, H.-Z. Lu, X. C. Xie, *Nat. Commun.* **2021**, *12*, 5038.
[19] A. Tiwari, F. Chen, S. Zhong, E. Drueke, J. Koo, A. Kaczmarek, C. Xiao, J. Gao, X. Luo, Q. Niu, Y. Sun, B. Yan, L. Zhao, A. W. Tsen, *Nat. Commun.* **2021**, *12*, 2049.
[20] P. He, G. K. W. Koon, H. Isobe, J. Y. Tan, J. Hu, A. H. C. Neto, L. Fu, H. Yang, *Nat. Nanotechnol.* **2022**, *17*, 378.
[21] M. Huang, Z. Wu, J. Hu, X. Cai, E. Li, L. An, X. Feng, Z. Ye, N. Lin, K. T. Law, N. Wang, *Natl. Sci. Rev.* **2022**, *10*, nwac232.
[22] S. Dzsaber, X. Yan, M. Taupin, G. Eguchi, A. Prokofiev, T. Shiroka, P. Blaha, O. Rubel, S. E. Grefe, H.-H. Lai, Q. Si, S. Paschen, *Proc. Natl. Acad. Sci. USA* **2021**, *118*, 2013386118.
[23] C.-L. Zhang, T. Liang, Y. Kaneko, N. Nagaosa, Y. Tokura, *npj Quantum Mater.* **2022**, *7*, 103.
[24] N. N. Orlova, A. V. Timonina, N. N. Kolesnikov, E. V. Deviatov, *Chin. Phys. Lett.* **2023**, *40*, 077302.
[25] A. Assoud, N. Soheilnia, H. Kleinke, *Intermetallics* **2007**, *15*, 371.
[26] D. Zhang, M. Shi, T. Zhu, D. Xing, H. Zhang, J. Wang, *Phys. Rev. Lett.* **2019**, *122*, 206401.
[27] J. Li, Y. Li, S. Du, Z. Wang, B.-L. Gu, S.-C. Zhang, K. He, W. Duan, Y. Xu, *Sci. Adv.* **2019**, *5*, aaw5685.
[28] M. M. Otrokov, I. I. Klimovskikh, H. Bentmann, D. Estyunin, A. Zeugner, Z. S. Aliev, S. Gaß, A. U. B. Wolter, A. V. Koroleva, A. M. Shikin, M. Blanco-Rey, M. Hoffmann, I. P. Rusinov, A. Y. Vyazovskaya, S. V. Eremeev, Y. M. Koroteev, V. M. Kuznetsov, F. Freyse, J. Sánchez-Barriga, I. R. Amiraslanov, M. B. Babanly, N. T. Mamedov, N. A. Abdullayev, V. N. Zverev, A. Alfonsov, V. Kataev, B. Büchner, E. F. Schwier, S. Kumar, A. Kimura, et al., *Nature* **2019**, *576*, 416.
[29] Y. Deng, Y. Yu, M. Z. Shi, Z. Guo, Z. Xu, J. Wang, X. H. Chen, Y. Zhang, *Science* **2020**, *367*, 895.
[30] C. Liu, Y. Wang, H. Li, Y. Wu, Y. Li, J. Li, K. He, Y. Xu, J. Zhang, Y. Wang, *Nat. Mater.* **2020**, *19*, 522.
[31] S. H. Lee, D. Graf, L. Min, Y. Zhu, H. Yi, S. Ciocys, Y. Wang, E. S. Choi, R. Basnet, A. Fereidouni, A. Wegner, Y.-F. Zhao, K. Verlinde, J. He, R. Redwing, V. Gopalan, H. O. H. Churchill, A. Lanzara, N. Samarth, C.-Z. Chang, J. Hu, Z. Q. Mao, *Phys. Rev. X* **2021**, *11*, 031032.
[32] S. H. Lee, D. Graf, R. Robinson, J. Singleton, J. C. Palmstrom, Z. Mao, *Phys. Rev. B* **2023**, *107*, 205105.
[33] A. Gao, Y.-F. Liu, C. Hu, J.-X. Qiu, C. Tzschaschel, B. Ghosh, S.-C. Ho, D. Bérubé, R. Chen, H. Sun, Z. Zhang, X.-Y. Zhang, Y.-X. Wang, N. Wang, Z. Huang, C. Felser, A. Agarwal, T. Ding, H.-J. Tien, A. Akey, J. Gardener, B. Singh, K. Watanabe, T. Taniguchi, K. S. Burch, D. C. Bell, B. B. Zhou, W. Gao, H.-Z. Lu, A. Bansil, et al., *Nature* **2021**, *595*, 521.

[34] J. L. Zhang, D. H. Wang, M. J. Shi, T. S. Zhu, H. J. Zhang, J. Wang, *Chin. Phys. Lett.* **2020**, *37*, 077304.
[35] R. Li, J. Wang, X.-L. Qi, S.-C. Zhang, *Nat. Phys.* **2010**, *6*, 284.
[36] V. O. Garlea, R. Jin, D. Mandrus, B. Roessli, Q. Huang, M. Miller, A. J. Schultz, S. E. Nagler, *Phys. Rev. Lett.* **2008**, *100*, 066404.
[37] X.-L. Qi, T. L. Hughes, S.-C. Zhang, *Phys. Rev. B* **2008**, *78*, 195424.
[38] H. Ishizuka, N. Nagaosa, *Nat. Commun.* **2020**, *11*, 2986.
[39] S. H. Lee, Y. Zhu, Y. Wang, L. Miao, T. Pillsbury, H. Yi, S. Kempinger, J. Hu, C. A. Heikes, P. Quarterman, W. Ratcliff, J. A. Borchers, H. Zhang, X. Ke, D. Graf, N. Alem, C.-Z. Chang, N. Samarth, Z. Mao, *Phys. Rev. Res.* **2019**, *1*, 012011.
[40] C. Wang, Y. Gao, D. Xiao, *Phys. Rev. Lett.* **2021**, *127*, 277201.
[41] T. Holder, D. Kaplan, R. Ilan, B. Yan, **2021**, arXiv:2111.07780.
[42] D.-F. Shao, S.-H. Zhang, G. Gurung, W. Yang, E. Y. Tsymbal, *Phys. Rev. Lett.* **2020**, *124*, 067203.
[43] H. Liu, J. Zhao, Y.-X. Huang, W. Wu, X.-L. Sheng, C. Xiao, S. A. Yang, *Phys. Rev. Lett.* **2021**, *127*, 277202.
[44] L. Min, Y. Zhang, Z. Xie, S. V. G. Ayyagari, L. Miao, Y. Onishi, S. H. Lee, Y. Wang, N. Alem, L. Fu, Z. Mao, *Nat. Mater.* **2024**, *23*, 1671.
[45] A. S. Gliozzi, M. Miniaci, A. O. Krushynska, B. Morvan, M. Scalerandi, N. M. Pugno, F. Bosia, *Sci. Rep.* **2019**, *9*, 9560.
[46] Z. Hu, L. Zhang, A. Chakraborty, G. D'Olimpio, J. Fujii, A. Ge, Y. Zhou, C. Liu, A. Agarwal, I. Vobornik, D. Farias, C.-N. Kuo, C. S. Lue, A. Politano, S.-W. Wang, W. Hu, X. Chen, W. Lu, L. Wang, *Adv. Mater.* **2023**, *35*, 2209557.
[47] The data that support the findings of this study are openly available, in ScholarSphere, https://doi.org/10.26207/a7e3-a797 (accessed: March 2025).
[48] B. C. Chakoumakos, H. Cao, F. Ye, A. D. Stoica, M. Popovici, M. Sundaram, W. Zhou, J. S. Hicks, G. W. Lynn, R. A. Riedel, *J. Appl. Crystallogr.* **2011**, *44*, 655.
[49] J. Rodríguez-Carvajal, *Phys. B* **1993**, *192*, 55.
[50] J. M. Perez-Mato, S. V. Gallego, E. S. Tasci, L. Elcoro, G. d. l. Flor, M. I. Aroyo, *Annu. Rev. Mater. Res.* **2015**, *45*, 217.
[51] G. Kresse, D. Joubert, *Phys. Rev. B* **1999**, *59*, 1758.
[52] J. P. Perdew, K. Burke, M. Ernzerhof, *Phys. Rev. Lett.* **1996**, *77*, 3865.
[53] S. L. Dudarev, G. A. Botton, S. Y. Savrasov, C. J. Humphreys, A. P. Sutton, *Phys. Rev. B* **1998**, *57*, 1505.
[54] I. Souza, N. Marzari, D. Vanderbilt, *Phys. Rev. B* **2001**, *65*, 035109.